Supplementary Information

Multi-H-Bonded Self-Assembled Superstructures for Ultrahigh-Capacity and Ultralong-Life All-Organic Ammonium-Ion Batteries

Pingxuan Liu,[a] Ziyang Song,[a]* Qi Huang,[c] Ling Miao,[a] Yaokang Lv,[d] Lihua Gan,[a,b]* Mingxian Liu[a,b]*

[a] *Shanghai Key Lab of Chemical Assessment and Sustainability, School of Chemical Science and Engineering, Tongji University, 1239 Siping Rd., Shanghai, 200092, P. R. China. E-mail: 2310240@tongji.edu.cn; ganlh@tongji.edu.cn; liumx@tongji.edu.cn*

[b] *State Key Laboratory of Cardiovascular Diseases and Medical Innovation Center, Shanghai East Hospital, School of Medicine, Tongji University, 150 Jimo Rd., Shanghai 200120, P. R. China.*

[c] *Institute for Electric Light Sources, School of Information Science and Technology, Fudan University, 220 Handan Rd., Shanghai 200438, P. R. China.*

[d] *College of Chemical Engineering, Zhejiang University of Technology, 18 Chaowang Rd., Hangzhou 310014, P. R. China.*

Table of Contents

Section S1 Experimental Section 4

1.1 Material Synthesis.

1.2 Characterizations.

1.3 Electrochemical Measurements.

Section S2 Supplementary Methods 7

2.1 Density Functional Theory (DFT) Calculation.

2.2 Optical Energy Gap.

2.3 Activation Energy.

2.4 Redox Electron Transfer Number.

2.5 Charge Storage Kinetics.

Section S3 Supplementing Characterizations 10

Fig. S1 Schematic supramolecular self-assembly of CA and HT into OSs.

Fig. S2 FT-IR spectra of CA, HT and OSs.

Fig. S3 A high-resolution TEM image of OSs.

Fig. S4 (a) Nitrogen sorption isotherm and (b) pore size distribution curve of OSs.

Fig. S5 Thermogravimetric analysis of OSs.

Fig. S6 SEM images of (a) CA and (b) HT.

Fig. S7 (a) SEM and (b) TEM images of OSs.

Section S4 Electrochemistry Analysis 13

Fig. S8 Schematic configuration of aqueous Zn||OSs battery, including a Zn metal anode, a OSs cathode, and an aqueous 3 M NH_4OTF/H_2O electrolyte.

Fig. S9 (a) GCD curves of OSs cathodes at different polymerization times in 3 M NH_4OTF/H_2O. (b) GCD curves at 0.2 A g^{-1} and (c, d) rate capacities of Zn||CA and Zn||HT batteries in NH_4OTF/H_2O electrolyte.

Fig. S10 Ragone plots of Zn||OSs battery in 3 M NH_4OTF/H_2O electrolyte based on the mass loading of OSs in the cathode (3 mg cm^{-2}).

Table S1 Comparison of specific capacity (mAh g^{-1}), energy density (Wh kg^{-1}), and cycling life of recently reported organic cathode materials of ZOBs in the literatures.

Fig. S11 GCD curve of Zn||OSs battery in 3 M $Zn(OTF)_2/H_2O$ electrolyte.

Fig. S12 (a) FT-IR spectra and (b) UV/Vis spectra of OSs cathodes before and after 60,000 cycles.

Fig. S13 (a, b) Top-view and (c) cross-sectional SEM images, and (d) XRD patterns of Zn anodes in Zn||OSs battery before and after long-term cycling.

Fig. S14 (a) Voltage profiles and (b) Coulombic efficiency of Zn||Cu cell in 3 M NH_4OTF electrolyte at a current density of 1 mA cm^{-2}.

Fig. S15 (a) *Ex-situ* XRD patterns and (b) *ex-situ* Raman spectra of OSs cathode in Zn||OSs battery at various electrochemical states.

Fig. S16 EIS spectra of OSs cathode at various temperatures (inset is a typical equivalent circuit, which includes the equivalent series resistance (R_s), charge transfer resistance (R_{ct}), Warburg impedance (Z_w) and constant phase angle element (CPE)). (b) Calculated R_{ct} values.

Fig. S17 GCD curves of Zn||OSs batteries in (a) NH_4OTF/H_2O electrolytes and (b) $HOTF/H_2O$ electrolytes with different pH values.

Fig. S18 A SEM image of OSs electrode at the fully discharged state in $HOTF/H_2O$ electrolyte (pH=4.85).

Fig. S19 (a) Element mapping images and (b) XPS spectra of OSs cathode in 3 M NH_4OTF/H_2O at full discharged state.

Fig. S20 GCD curves of Zn||graphite battery using 3 M NH_4OTF/H_2O electrolyte at 0.2 A g^{-1}.

Fig. S21 An optimized supramolecular model for MEP simulations of OSs.

Table S2 Comparison of specific capacity (mAh g^{-1}), energy density (Wh kg^{-1}) and cycling life of recently reported organic batteries in the literatures.

Section S5 References 28

Section S1 Experimental Section

1.1 Material Synthesis.

1,3,4,6,7,9,9b-heptaazaphenalen-2,5,8-triamin (HT, 98%), cyanuric acid (CA, 98%), and dimethyl sulfoxide (99.9%) were purchased from Sinopharm. All reagents were used as received, without further purification.

Firstly, HT (0.218 g, 0.001 mol) and CA (0.129 g, 0.001 mol) were dissolved in 100 mL dimethyl sulfoxide solvent, respectively. Both solutions were mixed together in a 500 mL flask by sonication treatment without inert atmosphere, and reacted for 60 minutes at room temperature. Subsequently, the reaction precipitates were sequentially filtered, washed with water and ethanol, and dried at 60 °C for 12 hours. The organic supramolecular precipitate products were obtained (named OSs).

1.2 Characterizations.

The material morphology and elemental distribution were examined using field-emission scanning electron microscopy (SEM, Hitachi S-4800) equipped with an X-ray energy dispersive spectroscopy (EDS) instrument and transmission electron microscopy (TEM, JEM-2100).

Fourier transform infrared (FT-IR) spectra were analyzed on a Thermo Nicolet NEXUS spectrometer.

Structural information of the materials was characterized by X-ray powder diffraction (XRD) analysis, collected by a diffractometer (Bruker D8 advance system) utilizing a Cu K radiation source, and through Raman spectrum (Renishaw Invia) under ambient conditions using 514 nm laser excitation.

Nitrogen adsorption-desorption measurements were performed using a Micromeritics ASAP 2460 apparatus at −196 °C. The surface area and pore size distribution were estimated through Brunauer-Emmett-Teller (BET) method and the nonlocal density functional theory model.

The ultraviolet visible (UV-Vis) spectra of the sample were collected by a UV-Vis spectrometer (JASCO V-750).

The thermal stability was monitored on a STA409 PC thermogravimetric (TG) analyzer in nitrogen atmosphere at a heating speed of 10 °C min^{-1}.

Surface functionality was measured by an X-ray photoelectron spectroscopy (XPS) with Al Kα radiation microscope. The electrical conductivity of the sample was measured via an RTS-8 four-point probe. With the addition of graphite conductive agent (30 wt%), OSs/CA/HT cathodes pressed into a thin sheet (1 cm in diameter, 0.1 cm in thickness) for the test.

For *ex-situ* spectroscopic characterizations, including FT-IR, XPS, XRD, SEM, Raman and UV-Vis, OSs cathodes were collected by disassembling batteries at specific voltages during (dis)charging/after cycling. The electrodes were then rinsed thoroughly with distilled water for 5 times to ensure the removal of adhered glass fiber and residual electrolyte. Finally, the electrodes were dried in a vacuum oven at 60 °C for 24 h.

1.3 Electrochemical Measurements.

The working electrode was prepared by mixing OSs, graphite and polytetrafluoroethylene (with a mass ratio of 6:3:1) using ethanol solvent to obtain the slurry, which was then coated onto the stainless-steel mesh (the mass loading of active substance is ~3 mg cm^{-2}) and dried in a vacuum oven at 80 °C for 12 h. Subsequently, a disc, which was received by flattening the slurry, was pressed on the stainless-steel mesh through a tablet press at 20 MPa. Finally, the cathode was obtained via vacuum drying the disc on the stainless-steel mesh. Aqueous Zn-ion organic batteries (ZOBs) were assembled in CR2032 coin cells at room temperature with Zn foil, OSs (or CA, HT, graphite), 3 mol L^{-1} $NH_4CF_3SO_3$ (denoted as NH_4OTF, 130 μL), glass fiber membrane as anode, cathode electrode, electrolyte, and separator, respectively. The typical current density for zinc anode is 1 mA cm^{-2}. OSs electrode was discharged to 0.2 V at 0.2 A g^{-1} to obtain a reduced state electrode (named OSs-R). To construct aqueous all-organic batteries (AOBs), OSs-R as the anode, OSs as the cathode, 3 mol L^{-1} NH_4OTF/H_2O solution as the electrolyte, and glass fiber separator (Whatman) were packaged into 2032 coin-type cells.

A CHI660E electrochemical workstation was employed to investigate the electrochemical performances of the devices including cyclic voltammetry (CV) and electrochemical impedance spectroscopy (EIS) (0.01 Hz to 100 kHz). The galvanostatic charge/discharge (GCD) measurement of Zn-ion devices was performed on a LAND-CT3002A system within the potential range from 0.2 to 1.5 V. The specific capacity (, mAh g^{-1}), energy density (E, Wh kg^{-1}) and power density (P, W kg^{-1}) were calculated from GCD curves using the following equations:

$$C_{\mathrm{m}} = \frac{I \times \Delta t}{m} \tag{Eq. S1}$$

$$E = C_{\mathrm{m}} \times \Delta V \tag{Eq. S2}$$

$$P = \frac{E}{1000 \times \Delta t} \tag{Eq. S3}$$

where I (A g^{-1}), Δt (s), m (g), ΔV (V) are the current density, discharge time, mass loading of active substance on the cathode and voltage window, respectively. Ragone plots of Zn||OSs battery (**Fig. S10** and **Fig. 2**c) were calculated by the integral areas of GCD curves at different current densities (**Fig. 2**a) based on the mass loading of OSs in the cathode (excluding the ammonium ion electrolyte).

Section S2 Supplementary Methods

2.1 Density Functional Theory (DFT) Calculation.

Supramolecular Property Simulation. The theoretical calculations were conducted using the Gaussian 16 program suite.[S1] The structures of OSs were optimized at the B3LYP-D3/def2-SVP level of theory. T The electrostatic potential (ESP) was analyzed, with negative ESP regions (red) indicating electrophilic sites and positive ESP regions (blue) representing nucleophilic sites. The π-electron localization function (ELL-π) was computed using Multiwfn 3.8 programs.[S2] The molecular orbital levels of OSs, including the highest occupied molecular orbital (HOMO) and the lowest unoccupied molecular orbital (LUMO), along with the charge population sum of OSs were investigated at the B3LYP-D3/TZVP level of theory. Density gradient (RDG) simulations[S3] were performed with the Multiwfn program to investigate the type of interaction force. Obviously, π-π stacking interactions is revealed when the value of sign(λ_2)ρ approaches zero.

Geometry optimization and Charge Density Difference. All the DFT calculations were carried out via the Vienna Ab initio Simulation Package (VASP)[S4] and the projector augmented wave (PAW) method.[S5] The exchange-functional was processed by using the generalized gradient approximation (GGA) with Perdew-Burke-Emzerhof (PBE) functional.[S6] The energy cutoff for the plane wave basis expansion was set to 400 eV. Partial occupation width of 0.2 eV was allowed for the Kohn−Sham orbitals via Gaussian smearing. The Brillourin zone was sampled using a 1×1×1 Monkhorst mesh during structural optimization. The convergence energy threshold for the self-consistent calculations was set to 10^{-4} eV, and the force convergency was set to 0.05 eV Å^{-1}. The charge density differences were analyzed by VASPKIT code. In order to quantitatively analyze the bonding properties of NH_4^+ adsorbed on organic superstructures (OSs) and characterization of charge transfer, the charge densities of NH_4^+ in the corresponding compounds were extracted from the corresponding charge densities in the OSs substrates to assess the differences in the charge densities of NH_4^+ adsorbed on the constructed OS models. The level of charge transfer between NH_4^+ and OSs was calculated using a Bader charge analysis program.[S7]

$$\Delta\rho = \rho(\mathrm{NH_4^+/OSs}) - \rho(\mathrm{OSs}) - \rho(\mathrm{NH_4^+}) \qquad \text{(Eq. S4)}$$

2.2 Optical Energy Gap.

The optical energy gaps (E_g, eV) of OSs cathodes can be measured by the UV-Vis spectroscopy, which are delivered as:[S8]

$$\alpha \propto \frac{(hv - E_g)^{1/2}}{hv} \quad \text{(Eq. S5)}$$

$$hv = 1280/\lambda \quad \text{(Eq. S6)}$$

where α denotes the optical absorption coefficient, hv is the photon energy, λ is the wavelength.

2.3 Activation Energy.

The activation energy (E_a, kJ mol^{-1}) for the charge transfer process can be obtained using the Arrhenius equation:[S9]

$$R_{ct}^{-1} = A\exp(-E_a/RT) \quad \text{(Eq. S7)}$$

where R_{ct} is the charge transfer resistance (Ω), A is constant under a stable experimental condition, R represents the gas constant (8.314 J mol^{-1} K^{-1}), and T is the temperature (K). The ln(R_{ct}^{-1}) values were drawed vs. 1000/T, and linear fitting was executed to gather E_a:

$$\ln(R_{ct}^{-1}) = -E_a/RT + k \quad \text{(Eq. S8)}$$

where k is constant.

2.4 Redox Electron Transfer Number.

The theoretical capacity (C_m, mAh g^{-1}) of OSs was calculated based on the following form:[S10]

$$C_m = \frac{n \times F}{3.6 \times M} \quad \text{(Eq. S9)}$$

The electron transfer number (n) during the coordination reaction was calculated according to the following equation:

$$n = \frac{3.6 \times C_m \times M}{F} \quad \text{(Eq. S10)}$$

where M is the molar mass of organic molecule (g mol^{-1}), and F is the Faraday constant (96485 C mol^{-1}).

2.5 Charge Storage Kinetics.

The charge storage kinetics of ZOBs were analyzed by CV curves at various scan rates. The relationship between the peak current (i) ans scan rate (v) was evaluated based on the equation:[S11]

$$i = kv^{\mathrm{b}} \qquad \text{(Eq. S11)}$$

where k and b are constants. The power exponent b is a crucial parameter in determining the charge storage kinetics during the redox process. The b-value of 0.5 and 1.0 indicate a diffusion-controlled step and a surface-governed procedure, respectively.

According to the Dunn's method, the contributions of the surface capacitive contribution and the diffusion-controlled process can be quantified by taking the following equation:[S12]

$$i = k_1 v + k_2 v^{1/2} \qquad \text{(Eq. S12)}$$

where k_1 and k_2 are constants, $k_1 v$ and $k_2 v^{1/2}$ represent the current density correlated with surface fast-capacitive reaction, and the current density due to diffusion-controlled reaction, respectively. After dividing both sides by $v^{1/2}$, the above equation is reformulated as below:

$$i/v^{1/2} = k_1 v^{1/2} + k_2 \qquad \text{(Eq. S13)}$$

The linear relationship between $i/v^{1/2}$ and $v^{1/2}$ can be obtained by means of a linear fit, where the slope of straight line is equal to k_1 and the y-intercept to k_2. Therefore, repeat the above steps for various voltages and scan rates to quantify the contribution of both charge storage.

Section S3 Supplementing Characterizations

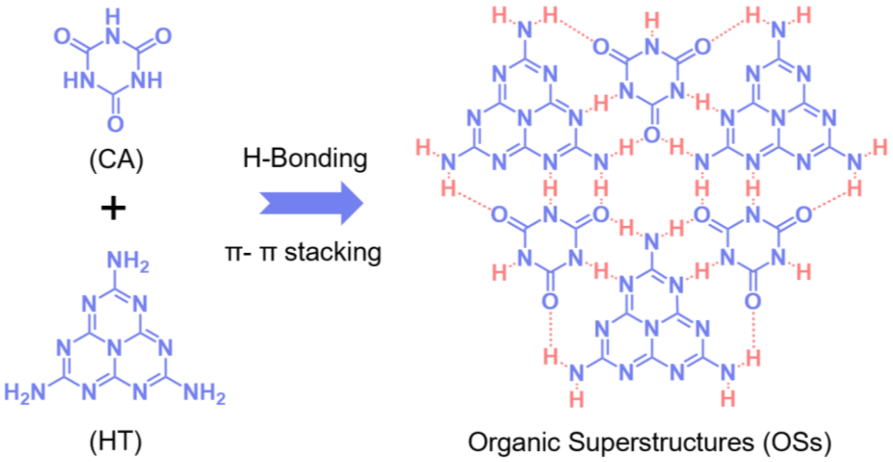

Fig. S1 Schematic supramolecular self-assembly of CA and HT into OSs.

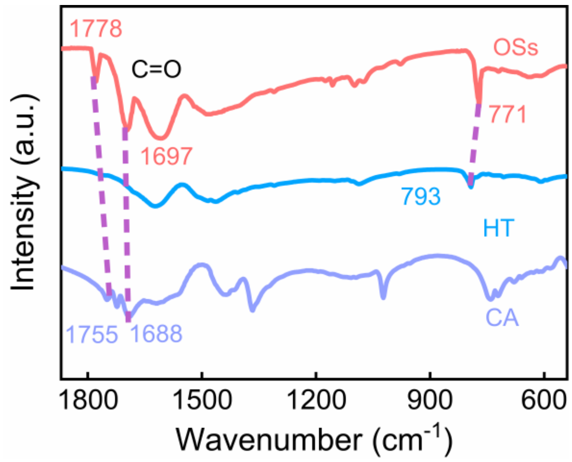

Fig. S2 FT-IR spectra of CA, HT and OSs.

Notes to Fig. S2: The C=O stretching vibrations of CA at 1688 and 1755 cm^{-1} are shifted to higher frequencies of 1697 and 1778 cm^{-1} in CA-HT, respectively. While the triazine ring vibration of HT moves from 793 to 771 cm^{-1} in CA-HT. The triazine ring vibration of HT shifts towards a lower frequency, while the C=O stretching vibration of CA shifts towards higher frequencies, suggesting the presence of H-bonding interactions of N−H···N and N−H···O between adjacent molecules.

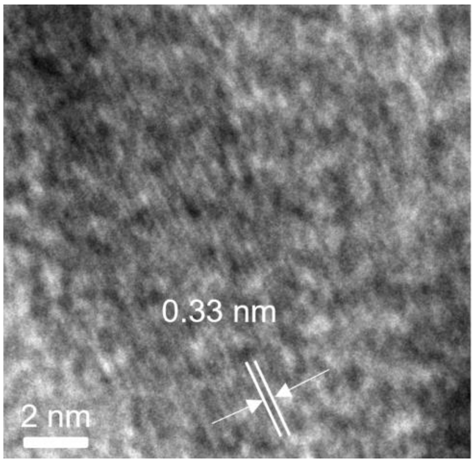

Fig. S3 A high-resolution TEM image of OSs.

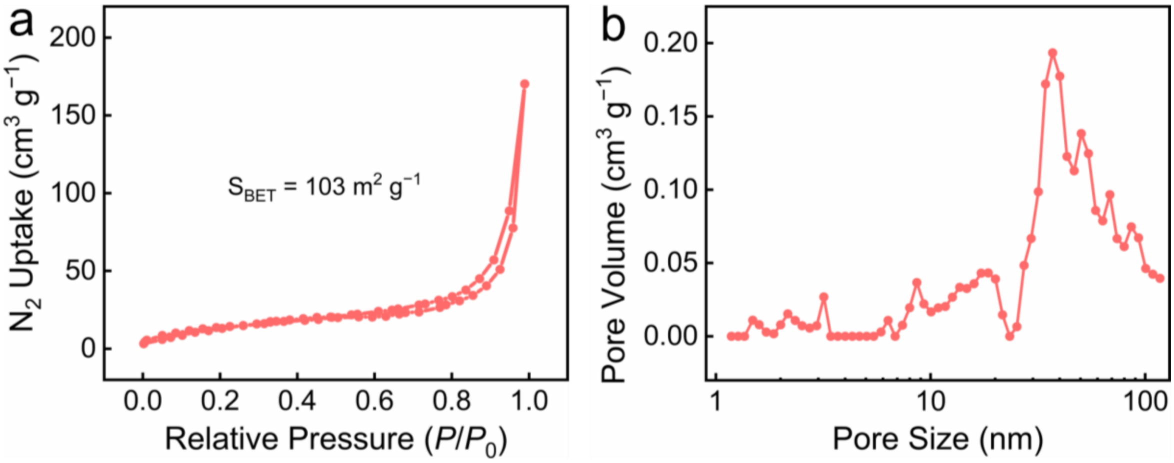

Fig. S4 (a) Nitrogen sorption isotherm and (b) pore size distribution curve of OSs.

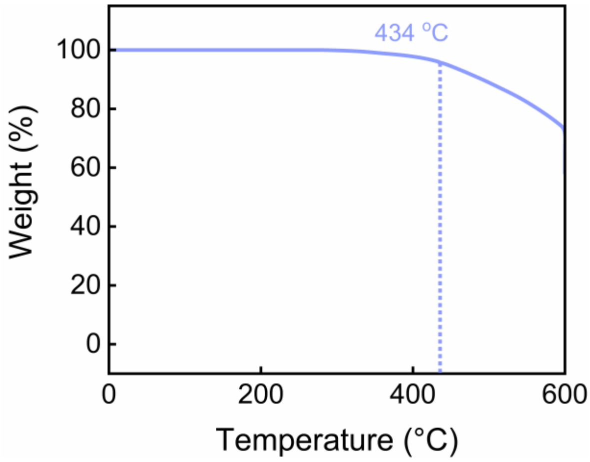

Fig. S5 Thermogravimetric analysis of OSs.

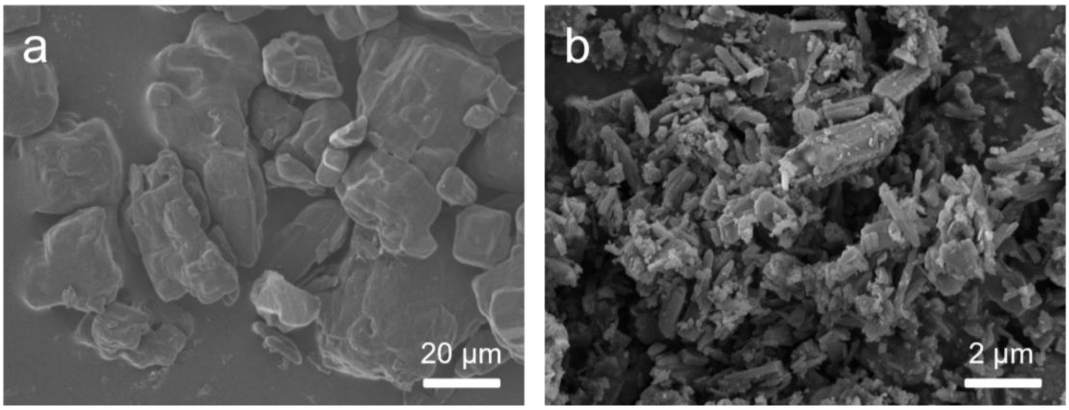

Fig. S6 SEM images of (a) CA and (b) HT.

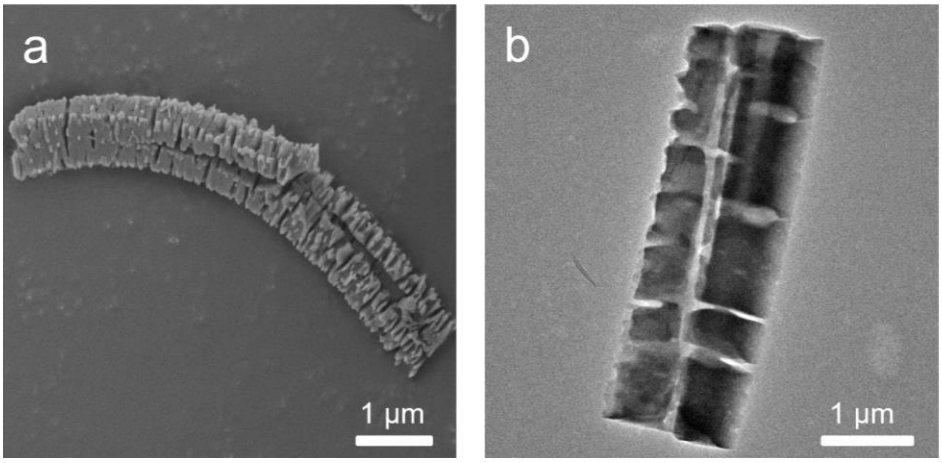

Fig. S7 (a) SEM and (b) TEM images of OSs.

Section S4 Electrochemistry Analysis

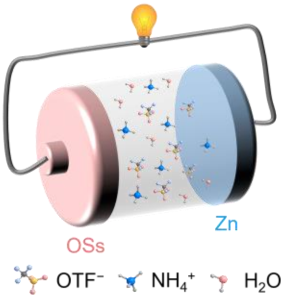

Fig. S8 Schematic configuration of aqueous Zn||OSs battery, including a Zn metal anode, a OSs cathode, and an aqueous 3 M NH_4OTF/H_2O electrolyte.

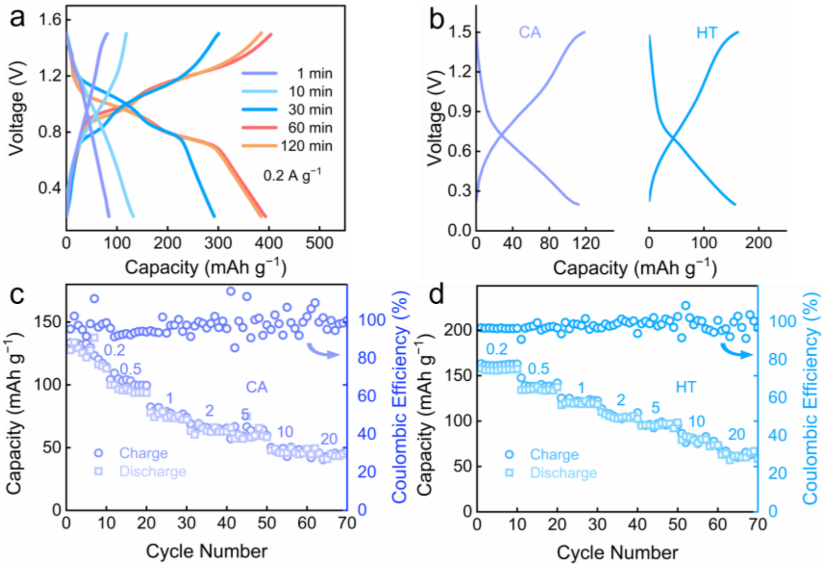

Fig. S9 (a) GCD curves of OSs cathodes at different polymerization times in 3 M NH_4OTF/H_2O. (b) GCD curves at 0.2 A g^{-1} and (c, d) rate capacities of Zn||CA and Zn||HT batteries in NH_4OTF/H_2O electrolyte.

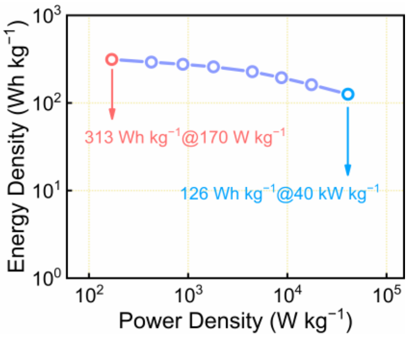

Fig. S10 Ragone plots of Zn||OSs battery in 3 M NH_4OTF/H_2O electrolyte based on the mass loading of OSs in the cathode (3 mg cm^{-2}).

Table S1 Comparison of specific capacity (mAh g^{-1}), energy density (Wh kg^{-1}), and cycling life of recently reported organic cathode materials of ZOBs in the literatures.

Materials	C_{m}	E	Life	Refs.
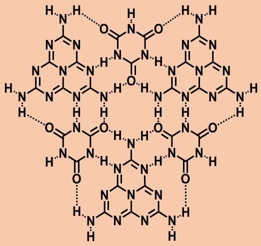 Organic Superstructures (OSs)	393@0.2 A g^{-1}	313	85.8%, 60,000 cycles, 10 A g^{-1}	This work
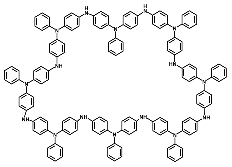 Polytriphenylamine (m-PTPA)	210.7@0.5 A g^{-1}	236	87.6%, 1000 cycles, 6 A g^{-1}	[S13]
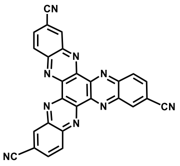 Cyano-Hexaazatrinnphthalene (HATN-3CN)	313@0.05 A g^{-1}	149.5	90.7%, 5800 cycles, 5 A g^{-1}	[S14]
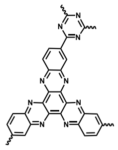 Triazine-linked Triquinoxalinylene Polymer (P3Q-t)	237@0.3 A g^{-1}	N/A	81%, 1500 cycles, 3 A g^{-1}	[S15]
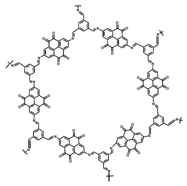 Orthoquinone-based Covalent Organic Framework (BT-PTO)	225@0.1 A g^{-1}	92.4	98%, 10,000 cycles, 5 A g^{-1}	[S16]

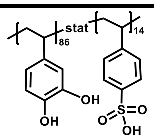 Poly(catechol) (P(4VC$_{86}$-stat-SS$_{14}$))	324@0.34 A g^{-1}	352	83%, 48,000 cycles, 9.4 A g^{-1}	[S17]
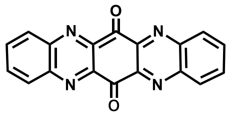 5,7,12,14-Tetraaza-6,13-pentacenequinone (TAPQ)	182@2 A g^{-1}	282	70%, 250 cycles, 0.05 A g^{-1}	[S18]
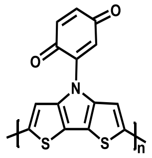 Poly(4-(2,5-hydroquinone)-4H-dithieno[3,2-b:2″,3″-d]pyrrole) (PDpBQH)	120@0.1 A g^{-1}	139	78%, 500 cycles, 2 A g^{-1}	[S19]
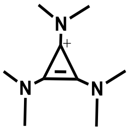 Trisaminocyclopropenium (CP^{+})	154.8@1 A g^{-1}	138	95%, 10,000 cycles, 2 A g^{-1}	[S20]
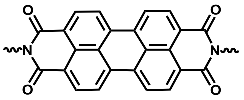 Polyimide (PI-1)	110@0.2 A g^{-1}	50.5	100%, 30,000 cycles, 10 A g^{-1}	[S21]
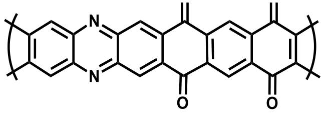 Poly(phenazine-alt-pyromellitic anhydride) (PPPA)	210@0.05 A g^{-1}	N/A	70.6%, 20,000 cycles, 0.05 A g^{-1}	[S22]
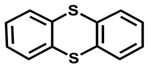 Thianthrene (TT)	66@0.2 A g^{-1}	67	82%, 8000 cycles, 1 A g^{-1}	[S23]

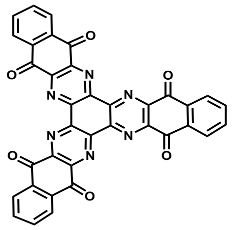 Hexaazatrinaphthalene-quione (HATNQ)	177.5@9 A g^{-1}	289	75%, 11,000 cycles, 5 A g^{-1}	[S24]
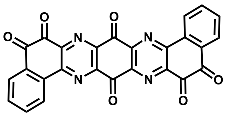 Benzo[a]benzo[7,8]quinoxalino[2,3-i]phenazine5,6,8,14,15,17-hexane (BBQPH)	498.6@0.2 A g^{-1}	355	95%, 1000 cycles, 5 A g^{-1}	[S25]
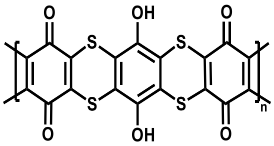 Polytetrafluorohydroquinone (PTFHQ)	211@1 A g^{-1}	355	92%, 3400 cycles, 20 A g^{-1}	[S26]
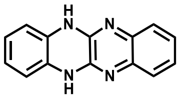 5,12-Dihydro-5,6,11,12-tetraazatetracene (DHTAT)	224@0.05 A g^{-1}	105.1	73%, 5000 cycles, 5 A g^{-1}	[S27]
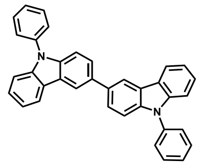 Dicarbazyl N-phenyl Carbazole Compound (dNPC)	100@0.05 A g^{-1}	100	96%, 1000 cycles, 0.5 A g^{-1}	[S28]
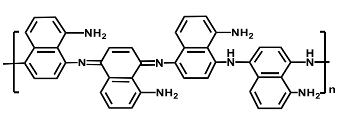 Poly(1,8-diaminonaphthalene) (PDAN)	171@0.1 A g^{-1}	121.1	82.3%, 10,000 cycles, 5 A g^{-1}	[S29]

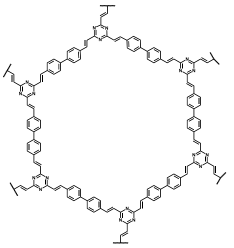 2,4,6-Trimethyl-1,3,5-triazine-4,4′-(benzothiadiazole-4,7-diyl)dibenzaldehyde (TMT-BT)	283.5@0.1 A g^{-1}	219.6	65.9%, 2000 cycles, 0.1 A g^{-1}	[S30]
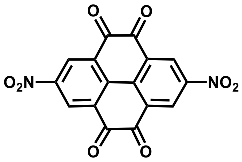 2, 7-Dinitropyrene-4, 5, 9, 10-tetraone (DNPT)	320@0.2 A g^{-1}	226	81.2%, 60000 cycles, 10 A g^{-1}	[S31]
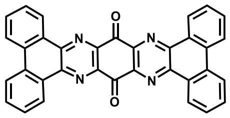 Dibenzo [a, c]-dibenzo [5, 6:7, 8]-quinoxalino [2, 3-i] phenazine-10, 21-dione (TABQ-PQ)	181.9@0.2 A g^{-1}	N/A	90.8%, 30000 cycles, 5 A g^{-1}	[S32]
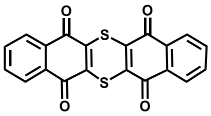 Dibenzo[b,i]thianthrene-5,7,12,14-tetraone (DTT)	211@0.05 A g^{-1}	126.5	83.8%, 23,000 cycles, 2 A g^{-1}	[S33]
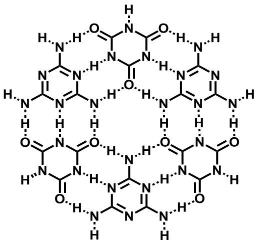 H-Bonded Organic Superstructures (HBOSs)	135@150 A g^{-1}	267	92.3%, 50,000 cycles, 10 A g^{-1}	[S34]

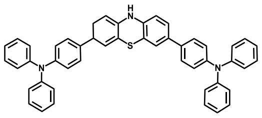 4,4′-(10*H*-phenothiazine-3,7-diyl) bis (N, N-diphenylaniline) (PTZAN)	145@0.1 A g^{-1}	187.2	77%, 2000 cycles, 1 A g^{-1}	[S35]
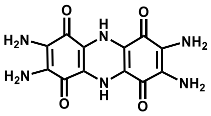 2,3,7,8-Tetraamino-5,10-dihydrophenazine-1,4,6,9-tetraone (TDT)	369@0.2 A g^{-1}	N/A	81.3%, 3000 cycles, 10 A g^{-1}	[S36]
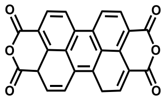 3,4,9,10-Perylenetetracarboxylic Dianhydride (π-PMC)	122.9@0.2 A g^{-1}	60	80.8%, 500 cycles, 8 A g^{-1}	[S37]
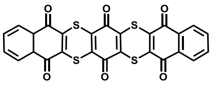 Benzo[b]naphtho[2’,3’:5,6][1,4]dithiino[2,3-i]thianthrene-5,7,9,14,16,18-hexone (BNDTH)	289@0.1 A g^{-1}	N/A	65%, 58,000 cycles, 10 A g^{-1}	[S38]
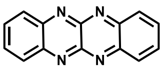 5,6,11,12-Tetraazanaphthacene (TANC)	213@0.5 C	245	71%, 47,500 cycles, 10 C	[S39]
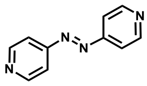 4,4’-Azopyridine (4,4’-AZPY)	266@0.5 C	291	100%, 60,000 cycles, 20 C	[S40]
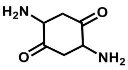 2,5-Diaminocyclohexa 2,5-diene-1,4-dione (DABQ)	376@0.1 A g^{-1}	N/A	100%, 1500 cycles, 5 A g^{-1}	[S41]

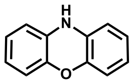 Phenoxazine (PNO)	215@0.05 A g^{-1}	N/A	100%, 3500 cycles, 2 A g^{-1}	[S42]
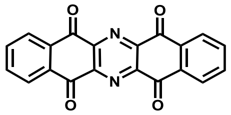 Dibenzo[b,i]- phenazine-5,7,12,14 tetrone (DPT)	366@0.1 A g^{-1}	176	87.1%, 12,000 cycles, 5 A g^{-1}	[S43]
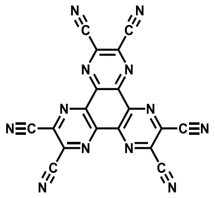 Dipyrazino[2,3-f:2′,3′-h]quinoxaline-2,3,6,7,10,11-hexacarbonitrile (DQH)	385@0.5 A g^{-1}	254	73.2%, 30,000 cycles, 10 A g^{-1}	[S44]
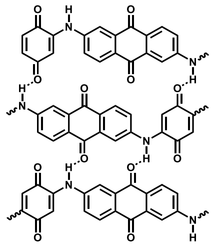 *p*-Benzo-quinone (BQ) and 2, 6-diaminoanthraquinone (DQ) OSs (BQ-DQ)	299@1 A g^{-1}	166	82.8%, 50,000 cycles, 10 A g^{-1}	[S45]

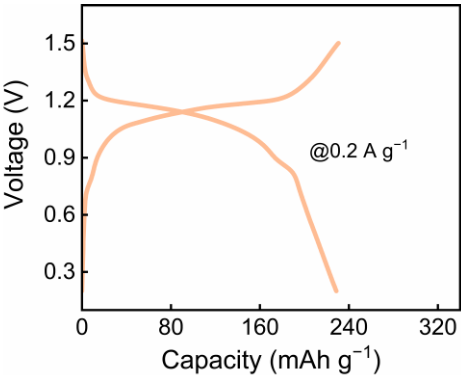

Fig. S11 GCD curve of Zn||OSs battery in 3 M Zn(OTF)$_2$/H_2O electrolyte.

Notes to Fig. S11: Zn||OSs battery in 3 M Zn(OTF)$_2$/H_2O electrolyte shows a high energy density of 219 Wh kg^{-1} based on the integral area of the GCD profile at 0.2 A g^{-1} (Fig. S11), which is much lower than that of 3 M NH_4OTF/H_2O electrolyte (313 Wh kg^{-1}, Figure 2c). This result highlights the superior redox charge storage of high-kinetics non-metallic NH_4^+ ions compared to larger-sized and slow metallic Zn^{2+} ions.

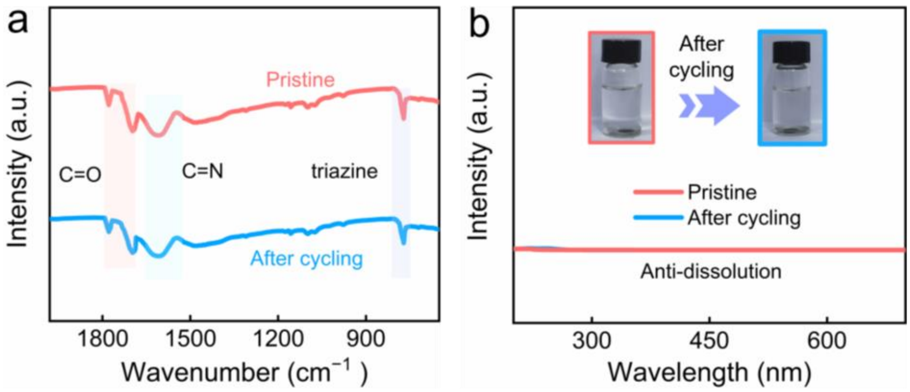

Fig. S12 (a) FT-IR spectra and (b) UV/Vis spectra of OSs cathodes before and after 60,000 cycles.

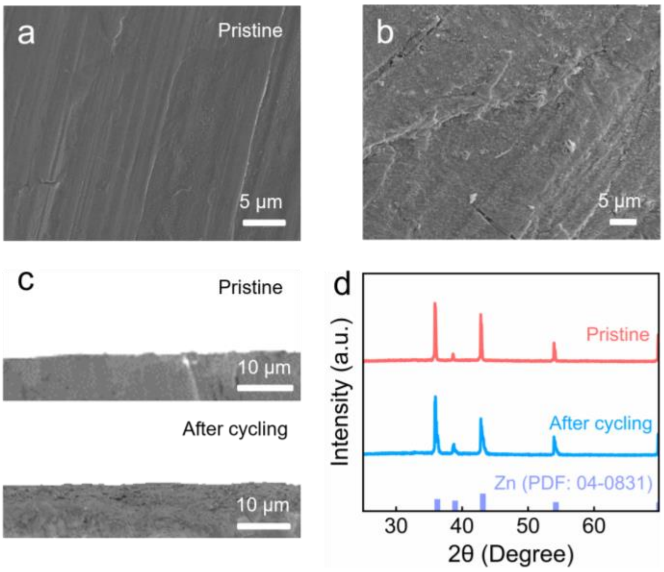

Fig. S13 (a, b) Top-view and (c) cross-sectional SEM images, and (d) XRD patterns of Zn anodes in Zn||OSs battery before and after long-term cycling.

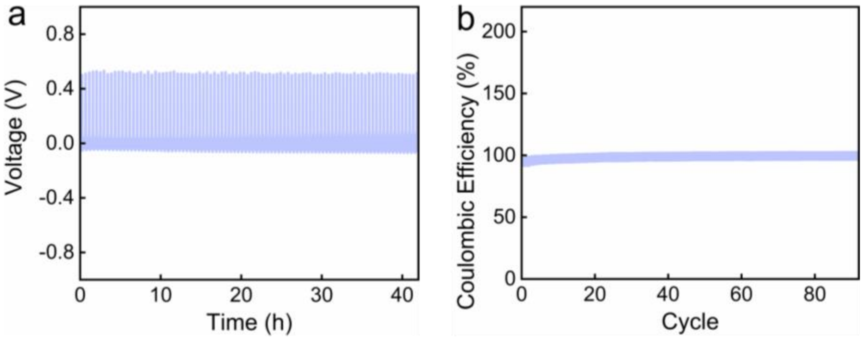

Fig. S14 (a) Voltage profiles and (b) Coulombic efficiency of Zn||Cu cell in 3 M NH_4OTF electrolyte at a current density of 1 mA cm^{-2}.

Notes to Fig. S14: Zn anode in aqueous 3 M NH_4OTF electrolyte achieves a Coulombic efficiency of 99.5% in Zn||Cu cell (Fig. S14), with a depth of discharge (DOD) of 11.1%.

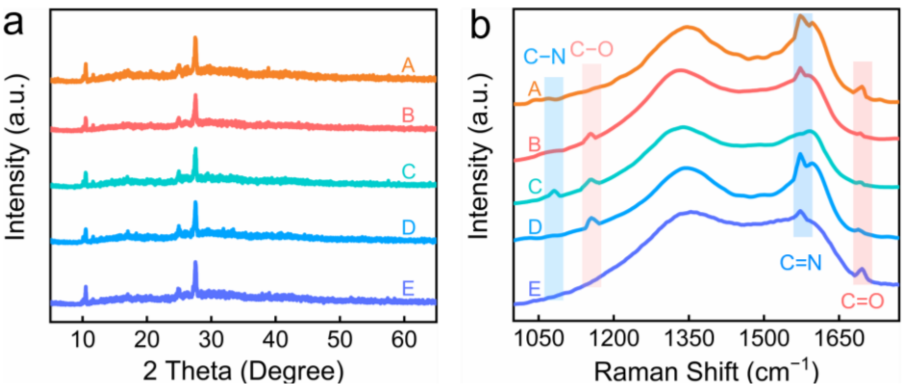

Fig. S15 (a) *Ex-situ* XRD patterns and (b) *ex-situ* Raman spectra of OSs cathode in Zn||OSs battery at various electrochemical states.

Notes to Fig. S15: *Ex-situ* XRD patterns (Fig. S15a) of OSs cathode are almost identical at different (dis)charging states of GCD profile (Fig. 3a), indicating its desirable structural stability during reversible NH_4^+ uptake/removal. In *ex-situ* Raman spectra (Fig. S15b), the signal of C=O gradually decreases during discharging (state A→B) due to NH_4^+ coordination, and is unchanged after subsequent discharging (state B→C), accompanied by the emergence of C−O signal. In contrast, the peak of C=N motifs is unchanged during discharging (state A→B) but declines in subsequent discharging (state B→C). Meanwhile, the generated C−N signal can be observed. Upon charging (state C→E), all signals revert to their initial levels, indicating NH_4^+ removal from C=O/C=N motifs of OSs cathode. Combined with FT-IR (Fig. 3b) and XPS analysis (Fig. 3c and d), these results imply that OSs cathode entails a successive two-step NH_4^+ coordination mechanism with C=O first followed by C=N motifs.

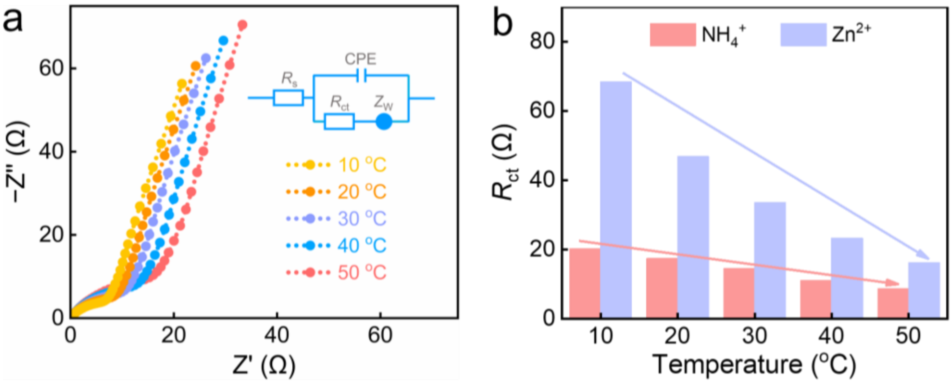

Fig. S16 EIS spectra of OSs cathode at various temperatures (inset is a typical equivalent circuit, which includes the equivalent series resistance (R_s), charge transfer resistance (R_{ct}), Warburg impedance (Z_w) and constant phase angle element (CPE)). (b) Calculated R_{ct} values.

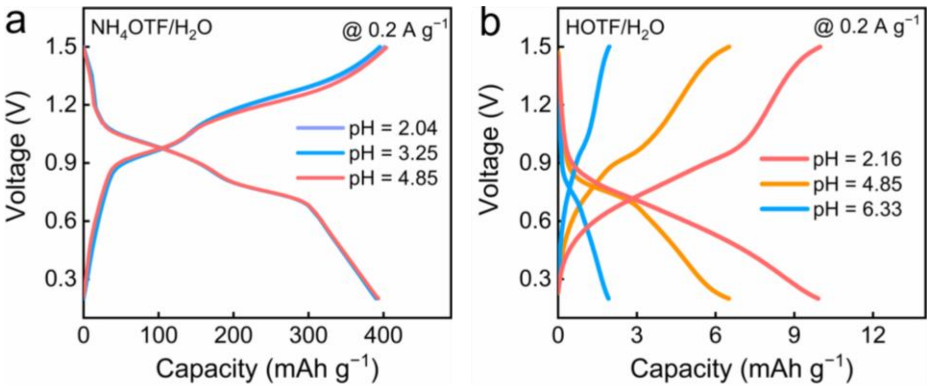

Fig. S17 GCD curves of Zn||OSs batteries in (a) NH_4OTF/H_2O electrolytes and (b) $HOTF/H_2O$ electrolytes with different pH values.

<u>Notes to Fig. S17</u>: The pH values of NH_4OTF/H_2O electrolytes were further controlled to 2.04 and 3.25 via adding $HOTF/H_2O$ solution to decouple H^+/NH_4^+ contributions and confirm NH_4^+-exclusive storage (Fig. S17). Zn||OSs batteries in these two electrolytes show high capacities (Fig. S17a) similar to the original NH_4OTF/H_2O electrolyte (pH=4.85), confirming the negligible contribution of H^+ during the NH_4^+-exclusive storage process. In addition, Zn||OSs batteries in $HOTF/H_2O$ electrolytes with different pH values (2.16, 4.85 and 6.33) display very low capacities (Fig. S17b), indicating the insignificant role of H^+ storage.

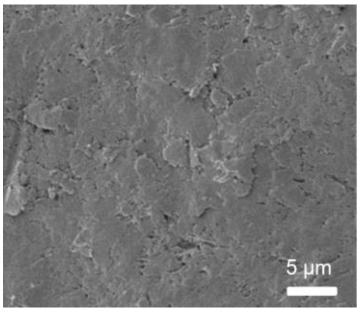

Fig. S18 A SEM image of OSs electrode at the fully discharged state in $HOTF/H_2O$ electrolyte (pH=4.85).

<u>Notes to Fig. S18</u>: As previously reported, the H^+ involvement as the charge carrier generate OH^- ions, which then react with Zn^{2+}, OTF^- and H_2O to form $Zn_4(OTF)_2(OH)_6\cdot xH_2O$ nanoflakes on the electrode surface. The absence of H^+ charge carrier is also reflected by the exclusion of $Zn_4(OTF)_2(OH)_6\cdot xH_2O$ nanoflakes on the surface of OSs cathode at the fully discharged state. Thus, it can be concluded that NH_4^+ ions dominate the charge storage in OSs cathode during the (dis)charge process.

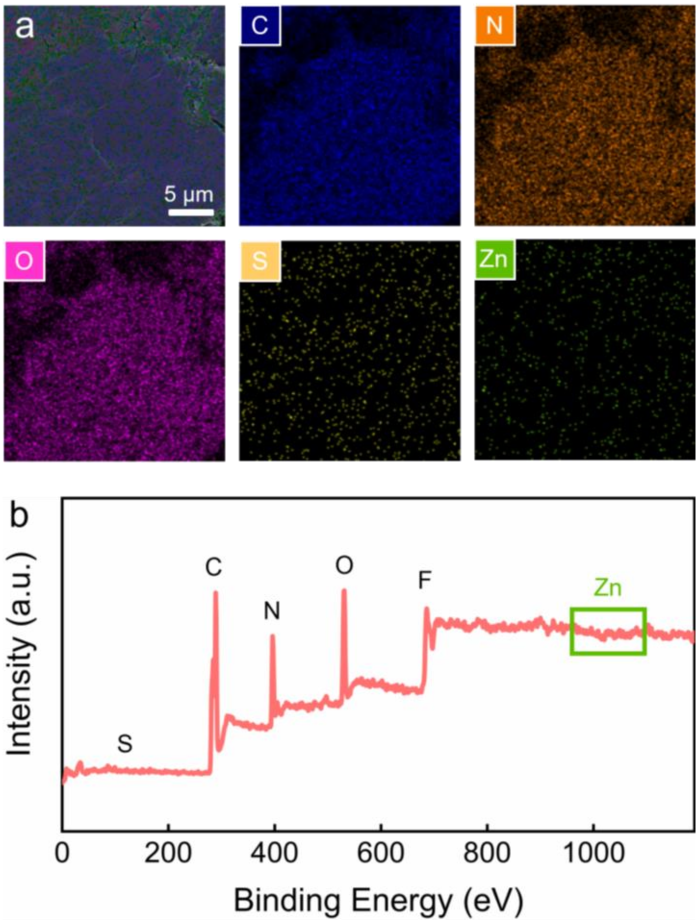

Fig. S19 (a) Element mapping images and (b) XPS spectra of OSs cathode in 3 M NH_4OTF/H_2O at full discharged state.

Notes to Fig. S19: Element mapping images of OSs cathode exhibits weak distribution signal of Zn element, with a content of 0.01 wt%. Similar phenomenon was also reported in the literature [S10]. XPS spectrum also confirms the very low Zn content of 0.10 wt%, indicating that Zn^{2+} ions do not insert into OSs cathode to storage energy.

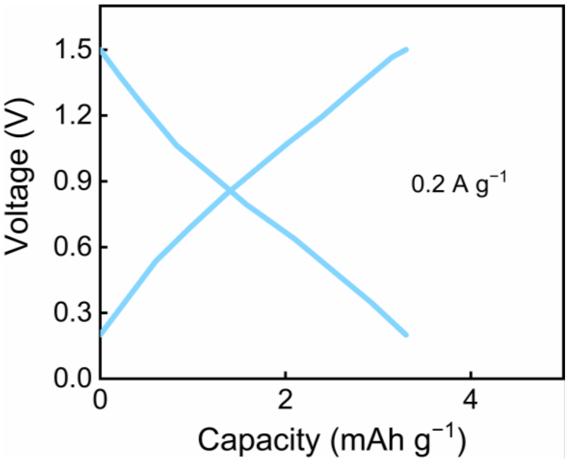

Fig. S20 GCD curves of Zn||graphite battery using 3 M NH_4OTF/H_2O electrolyte at 0.2 A g^{-1}.

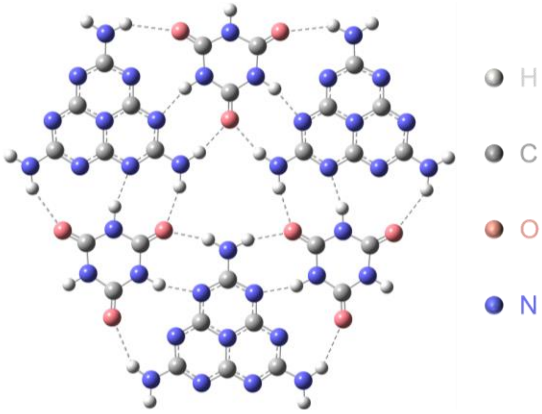

Fig. S21 An optimized supramolecular model for MEP simulations of OSs.

Table S2 Comparison of specific capacity (mAh g^{-1}), energy density (Wh kg^{-1}) and cycling life of recently reported organic batteries in the literatures.

System	Electrolyte	C_m	E	Lifespan	Refs.
OSs||OSs-R	3 M NH_4OTF	213@0.2 A g^{-1} 96@50 A g^{-1}	80.9	90.3%, 100,000 cycles, 5 A g^{-1}	This Work
GDAQ||GDAQ-R	2 M $ZnSO_4$	141@0.1 A g^{-1} ~80@10 A g^{-1}	26.8	92.5%, 5000 cycles, 1 A g^{-1}	[S46]
QDPA||NPI	2 M $ZnSO_4$	189@0.1 A g^{-1} 77@5 A g^{-1}	43.1	70%, 1000 cycles, 1 A g^{-1}	[S47]
PR||PO	2 M $ZnSO_4$	147@0.1 A g^{-1} 90@2 A g^{-1}	88.2	94%, 500 cycles, 1 A g^{-1}	[S48]
PTDBS||PIND	0.5 M $MgCl_2$	101@0.8 A g^{-1} ~42@6 A g^{-1}	94.2	80%, 10,000 cycles, 4 A g^{-1}	[S49]
D-HATN||HSA	0.5 M H_2SO_4	150@1 A g^{-1} 100@10 A g^{-1}	41.2	59.8%, 500cycles, 5 A g^{-1}	[S50]
PUQ||PTC(QH_2)	0.5 M H_2SO_4	78@0.5 A g^{-1} 51@25 A g^{-1}	56.2	80%, 1000 cycles, 2 A g^{-1}	[S51]
TABQ||TCBQ	0.5 M H_2SO_4	176@1 A g^{-1} 104@30 A g^{-1}	18.1	71.2%, 3500 cycles, 5 A g^{-1}	[S52]
AQ||TPAD-COF	1.2 M H_2SO_4	111@0.5 A g^{-1} ~36@6 A g^{-1}	61.1	74%, 1000 cycles, 2 A g^{-1}	[S53]
HATP-PT COF||CuHCF	2.0 M NH_4OTf@S	97@0.4 A g^{-1} 87@5 A g^{-1}	30	89%, 20,000 cycles, 1 A g^{-1}	[S54]
PTCDI||N-CuHCF	5.8 M $(NH_4)_2SO_4$	48@5 C 39@20 C	63.1	72%, 1000 cycles, 10 C	[S55]
PTCDI||$VOPO_4 \cdot 2\,H_2O$	NH_4OTF /Acetonitrile	55@0.1 A g^{-1}	N/A	99.6%, 500 cycles, 0.1 A g^{-1}	[S56]

PNNI||Ni-APW	1 M NH$_4$Ac	67@0.3 A g^{-1} 44@2 A g^{-1}	N/A	100%, 10,000 cycles, 1 A g^{-1}	[S57]
PTCDI||A-MnPBA	MEE	116@0.5 A g^{-1} 62@10 A g^{-1}	65	73.9%, 10,000 cycles, 10 A g^{-1}	[S58]
PTCDI||MnHCF	1 M NH$_4$TFSI	45@0. 015 A g^{-1} 10@0.25 A g^{-1}	N/A	~71.1%, 70 cycles, 0.03 A g^{-1}	[S59]
PTCDI||MnAl-LDH	0.5 M (NH$_4$)$_2$SO$_4$	57@0.1 A g^{-1} 35@5 A g^{-1}	45.8	92%, 100 cycles, 0.1 A g^{-1}	[S60]
PTCDI||A-PBA	21 M NH$_4$TFSI	51@0.04 A g^{-1} ~27@6.4 A g^{-1}	55.5	72.3%, 4000 cycles, 0.4 A g^{-1}	[S61]
PTCDI@MXene||CuHCF	2 M NH$_4$OTf@S	41@0.2 A g^{-1} 23@1 A g^{-1}	41.5	77%, 2000 cycles, 0.5 A g^{-1}	[S62]
PTCDI||FeMnHCF	24 M NH$_4$OTF	124@0.5 A g^{-1} ~17@70 A g^{-1}	71	67%, 3000 cycles, 9 A g^{-1}	[S63]
PTCDI||Cu-HHTP-THBQ	3 M (NH$_4$)$_2$SO$_4$	132@0.2 A g^{-1} 71.2@10 A g^{-1}	N/A	88.2%, 12,000 cycles, 1 A g^{-1}	[S64]

Section S5 References

[S1] M. J. Frisch, G. W. Trucks, H. B. Schlegel, et al., Gaussian 16 Revision. A.03, Gaussian Inc., Wallingford, CT, **2016**.

[S2] T. Lu, F. Chen, *J. Comp. Chem.* **2012**, *33*, 580.

[S3] E. R. Johnson, S. Keinan, P. Mori-Sánchez, J. Contreras-García, A. J. Cohen, W. Yang, *J. Am. Chem. Soc.* **2010**, *132*, 6498.

[S4] G. Kresse, J. Furthmüller, *Comp. Mater. Sci.* **1996**, *6*, 15.

[S5] P. E. Blöchl, *Phys Rev B Condens Matter.* **1994**, *50*, 17953.

[S6] J. P. Perdew, J. A. Chevary, S. H. Vosko, K. A. Jackson, M. R. Pederson, D. J. Singh, C. Fiolhais, *Phys. Rev. B* **1992**, *46*, 6671.

[S7] N. Zhang, A. Jalil, D. Wu, S. Chen, Y. Liu, C. Gao, W. Ye, Z. Qi, H. Ju, C. Wang, X. Wu, L. Song, J. Zhu, Y. Xiong, *J. Am. Chem. Soc*. **2018**, *140,* 9434.

[S8] Z. Lin, H.-Y. Shi, L. Lin, X. Yang, W. Wu, X. Sun, *Nat. Commun.* **2021**, *12*, 4424.

[S9] L. Xie, K. Xu, W. Sun, Y. Fan, J. Zhang, Y. Zhang, H. Zhang, J. Chen, Y. Shen, F. Fu, H. Kong, G. Wu, J. Wu, L. Chen, H. Chen, *Angew. Chem. Int. Ed.* **2023**, *62*, e202300372.

[S10] Z. Tie, L. Liu, S. Deng, D. Zhao, Z. Niu, *Angew. Chem. Int. Ed.* **2020**, *59*, 4920.

[S11] Z. Song, L. Miao, L. Ruhlmann, Y. Lv, D. Zhu, L. Li, L. Gan, M. Liu, *Adv. Funct. Mater.* **2022**, *32*, 2208049.

[S12] M. Huang, Q. He, J. Wang, X. Liu, F. Xiong, Y. Liu, R. Guo, Y. Zhao, J. Yang, L. Mai, *Angew. Chem. Int. Ed.* **2023**, *62*, e202218922.

[S13] H. Zhang, L. Zhong, J. Xie, F. Yang, X. Liu, X. Lu, *Adv. Mater.* **2021**, *33*, 2101857.

[S14] Z. Ye, S. Xie, Z. Cao, L. Wang, D. Xu, H. Zhang, J. Matz, P. Dong, H. Fang, J. Shen, M. Ye, *Energy Storage Mater.* **2021**, *37*, 378.

[S15] X. Wang, J. Tang, W. Tang, *Adv. Funct. Mater.* **2022**, *32*, 2200517.

[S16] S. Zheng, D. Shi, D. Yan, Q. Wang, T. Sun, T. Ma, L. Li, D. He, Z. Tao, J. Chen, *Angew. Chem. Int. Ed.* **2022**, *61*, e202117511.

[S17] N. Patil, C. de la Cruz, D. Ciurduc, A. Mavrandonakis, J. Palma, R. Marcilla, *Adv. Energy Mater.* **2021**, *11*, 2100939.

[S18] Y. Gao, G. Li, F. Wang, J. Chu, P. Yu, B. Wang, H. Zhan, Z. Song, *Energy Storage Mater.* **2021**, *40*, 31.

[S19] X. Wang, J. Xiao, W. Tang, *Adv. Funct. Mater.* **2022**, *32*, 2108225.

[S20] Y. Yan, P. Li, Y. Wang, L. Bi, T. W. Lau, M. Miao, S. Yang, Q. Xiong, F. R. Lin, H.-L. Yip, J. Yin, C. Zhi, A. K. Y. Jen, *Adv. Funct. Mater.* **2024**, *34*, 2312332.

[S21] Z. Xu, M. Li, W. Sun, T. Tang, J. Lu, X. Wang, *Adv. Mater.* **2022**, *34*, 2200077.

[S22] F. Ye, Q. Liu, H. Dong, K. Guan, Z. Chen, N. Ju, L. Hu, *Angew. Chem. Int. Ed.* **2022**, *61*, e202214244.

[S23] H. Cui, T. Wang, Z. Huang, G. Liang, Z. Chen, A. Chen, D. Wang, Q. Yang, H. Hong, J. Fan, C. Zhi, *Angew. Chem. Int. Ed.* **2022**, *61*, e202203453.

[S24] Y. Chen, J. Li, Q. Zhu, K. Fan, Y. Cao, G. Zhang, C. Zhang, Y. Gao, J. Zou, T. Zhai, C. Wang, *Angew. Chem. Int. Ed.* **2022**, *61*, e202116289.

[S25] W. Li, H. Xu, H. Zhang, F. Wei, L. Huang, S. Ke, J. Fu, C. Jing, J. Cheng, S. Liu, *Nat. Commun.* **2023**, *14*, 5235.

[S26] Q.-Q. Sun, T. Sun, J.-Y. Du, Z.-L. Xie, D.-Y. Yang, G. Huang, H.-M. Xie, X.-B. Zhang, *Angew. Chem. Int. Ed.* **2023**, *62*, e202307365.

[S27] Y. Zhang, M. Li, Z. Li, Y. Lu, H. Li, J. Liang, X. Hu, L. Zhang, K. Ding, Q. Xu, H. Liu, Y. Wang, *Angew. Chem. Int. Ed.* **2024**, *63*, e202410342.

[S28] U. Mittal, F. Colasuonno, A. Rawal, M. Lessio, D. Kundu, *Energy Storage Mater.* **2022**, *46*, 129.

[S29] L. Yan, Q. Zhu, Y. Qi, J. Xu, Y. Peng, J. Shu, J. Ma, Y. Wang, *Angew. Chem. Int. Ed.* **2022**, *61*, e202211107.

[S30] H. Peng, S. Huang, V. Montes-García, D. Pakulski, H. Guo, F. Richard, X. Zhuang, P. Samorì, A. Ciesielski, *Angew. Chem. Int. Ed.* **2023**, *62*, e202216136.

[S31] Z. Song, L. Miao, Y. Lv, L. Gan, M. Liu, *Angew. Chem. Int. Ed.* **2023**, *62*, e202309446.

[S32] T. Sun, W. Zhang, Z. Zha, M. Cheng, D. Li, Z. Tao, *Energy Storage Mater.* **2023**, *59*, 102778.

[S33] Y. Wang, C. Wang, Z. Ni, Y. Gu, B. Wang, Z. Guo, Z. Wang, D. Bin, J. Ma, Y. Wang, *Adv. Mater.* **2020**, *32*, 2000338.

[S34] Z. Song, L. Miao, L. Ruhlmann, Y. Lv, L. Li, L. Gan, M. Liu, *Angew. Chem. Int. Ed.* **2023**, *62*, e202219136.

[S35] X. Qiu, J. Xu, K. Zhou, X. Huang, M. Liao, Y. Cao, G. Zhou, P. Wei, Y. Wang, *Angew. Chem. Int. Ed.* **2023**, *62*, e202304036.

[S36] L. Lin, Z. Lin, J. Zhu, K. Wang, W. Wu, T. Qiu, X. Sun, *Energy Environ. Sci.* **2023**, *16*, 89.

[S37] H. Zhang, Y. Fang, F. Yang, X. Liu, X. Lu, *Energy Environ. Sci.* **2020**, *13*, 2515.

[S38] Q.-Q. Sun, T. Sun, J.-Y. Du, K. Li, H.-M. Xie, G. Huang, X.-B. Zhang, *Adv. Mater.* **2023**, *35*, 2301088.

[S39] D. Du, J. Zhou, Z. Yin, G. Feng, W. Ji, H. Huang, S. Pang, *Adv. Energy Mater.* **2024**, *14*, 2400580.

[S40] D. Du, Y. Chen, H. Zhang, J. Zhao, L. Jin, W. Ji, H. Huang, S. Pang, *Angew. Chem. Int. Ed.* **2024**, *63*, e202408292.

[S41] J. Guo, J.-Y. Du, W.-Q. Liu, G. Huang, X.-B. Zhang, *Angew. Chem. Int. Ed.* **2024**, *63*, e202406465.

[S42] J. Ning, X. Zhang, D. Xie, Q. He, J. Hu, J. Tang, R. Li, H. Meng, K. X. Yao, *Angew. Chem. Int. Ed.* **2024**, *63*, e202319796.

[S43] X. Huang, X. Qiu, W. Wang, J. Li, Z. Li, X. Yu, J. Ma, Y. Wang, *J. Am. Chem. Soc.* **2023**, *145*, 25604.

[S44] Y. Zhang, Z. Song, L. Miao, Y. Lv, L. Gan, M. Liu, *Adv. Funct. Mater.* **2024**, *34*, 2405710.

[S45] Y. Zhang, Z. Song, L. Miao, Y. Lv, L. Gan, M. Liu, *Angew. Chem. Int. Ed.* **2024**, *63*, e202316835.

[S46] P. Yi, Z. Li, L. Ma, B. Feng, Z. Liu, Y. Liu, W. Lu, S. Cao, H. Fang, M. Ye, J. Shen, *Adv. Mater.* **2024**, *36*, 2414379.

[S47] J. Yang, H. Hua, H. Yang, P. Lai, M. Zhang, Z. Lv, Z. Wen, C. C. Li, J. Zhao, Y. Yang, *Adv. Energy Mater.* **2023**, *13*, 2204005.

[S48] Z. Tie, S. Deng, H. Cao, M. Yao, Z. Niu, J. Chen, *Angew. Chem. Int. Ed.*, **2022**, *61*, e202115180.

[S49] Z. Fu, H. Zhang, D. Geng, Z. Liu, Z. Zhang, X. Li, C. Yan, *Adv. Energy Mater.* **2024**, *36*, 2403934.

[S50] L. Zhong, C. Liu, Y. Zhang, J. Li, F. Yang, Z. Zhang, D. Yu, *Angew. Chem. Int. Ed.* **2025**, *64*, e202413971.

[S51] M. Zhu, L. Zhao, Q. Ran, Y. Zhang, R. Peng, G. Lu, X. Jia, D. Chao, C. Wang, *Adv. Sci.* **2022**, *9*, 2103896.

[S52] S. Wu, M. Taylor, H. Guo, S. Wang, C. Han, J. Vongsvivut, Q. Meyer, Q. Sun, J. Ho, C. Zhao, *Angew. Chem. Int. Ed.* **2024**, *63*, e202412455.

[S53] X. Yan, F. Wang, X. Su, J. Ren, M. Qi, P. Bao, W. Chen, C. Peng, L. Chen, *Adv. Mater.* **2023**, *35*, 2305037.

[S54] Z. Tian, V. S. Kale, S. Thomas, S. Kandambeth, I. Nadinov, Y. Wang, W. Wahyudi, Y. Lei, A.-H. Emwas, M. Bonneau, O. Shekhah, O. M. Bakr, O. F. Mohammed, M. Eddaoudi, H. N. Alshareef, *Adv. Mater.* **2024**, *36*, 2409354.

[S55] J. Han, M. Zarrabeitia, A. Mariani, M. Kuenzel, A. Mullaliu, A. Varzi, S. Passerini, *Adv. Mater.* **2022**, *34*, 2201877.

[S56] F. Ye, R. Pang, C. Lu, Q. Liu, Y. Wu, R. Ma, L. Hu, *Angew. Chem. Int. Ed.* **2023**, *62*, e202303480.

[S57] S. Zhang, K. Zhu, Y. Gao, D. Cao, *ACS Energy Lett.* **2023**, *8*, 889.

[S58] H. Hong, J. Zhu, Y. Wang, Z. Wei, X. Guo, S. Yang, R. Zhang, H. Cui, Q. Li, D. Zhang, C. Zhi, *Adv. Mater.* **2024**, *36*, 2308210.

[S59] H. Zhang, Y. Tian, W. Wang, Z. Jian, W. Chen, *Angew. Chem. Int. Ed.* **2022**, *61*, e202204351.

[S60] Q. Liu, F. Ye, K. Guan, Y. Yang, H. Dong, Y. Wu, Z. Tang, L. Hu, *Adv. Energy Mater.* **2023**, *13*, 2202908.

[S61] L. Chen, W. Sun, K. Xu, Q. Dong, L. Zheng, J. Wang, D. Lu, Y. Shen, J. Zhang, F. Fu, H. Kong, J. Qin, H. Chen, *ACS Energy Lett.* **2022**, *7*, 1672.

[S62] Z. Tian, J. Yin, T. Guo, Z. Zhao, Y. Zhu, Y. Wang, J. Yin, Y. Zou, Y. Lei, J. Ming, O. Bakr, O. F. Mohammed, H. N. Alshareef, *Angew. Chem. Int. Ed.* **2022**, *61*, e202213757.

[S63] L. Du, S. Bi, M. Yang, Z. Tie, M. Zhang, Z. Niu, *Proc. Natl. Acad. Sci.* **2022**, *119*, e2214545119.

[S64] H. Lu, J. Hu, K. Zhang, Y. Zhang, B. Jiang, M. Zhang, S. Deng, J. Zhao, H. Pang, B. Xu, *Adv. Mater.* **2024**, *36*, 2408396.